Scalar Power Spectra and Scalar Structure Function Evolution in the Richtmyer-Meshkov Instability Upon Re-Shock

Christopher D. Noble*
Graduate Research Assistant
Wisconsin Shock Tube Laboratory
Department of Engineering Physics
University of Wisconsin - Madison
Madison, Wisconsin 53706
Email: cdnoble@wisc.edu

Josh M. Herzog
Graduate Research Assistant
David A. Rothamer
Professor
Engine Research Center
Department of Mechanical Engineering
University of Wisconsin - Madison
Madison, Wisconsin 53706

Alex M. Ames
Graduate Research Assistant
Jason Oakley
Research Scientist
Riccardo Bonazza
Professor
Wisconsin Shock Tube Laboratory
Department of Engineering Physics
University of Wisconsin - Madison
Madison, Wisconsin 53706

ABSTRACT

The Richtmyer-Meshkov instability (RMI) of a twice-shocked gas interface is studied using high-speed planar laser-induced fluorescence (PLIF) in the Wisconsin Shock Tube Laboratory's vertical shock tube. The initial condition (IC) is a shear layer with broadband diffuse perturbations at the interface between a helium-acetone mixture and argon. This IC is accelerated by a shock of nominal strength $M = 1.9$, and then accelerated again by the transmitted shock that reflects off the end wall of the tube. Three individual experiments are analyzed, the energy spectrum and the structure functions of the light gas mole fraction field are calculated and compared.

Nomenclature

ξ Light gas mole fraction
h Mixing thickness
k_x^* Dimensionless wavenumber in the spanwise direction
r_x^* Dimensionless two-point separation in the spanwise direction
E_ξ Scalar power spectrum
Λ_ξ Integrated scalar power spectrum
$S_{\xi,p}$ p^{th}-order scalar structure function
$Z_{\xi,p}$ Integrated p^{th}-order scalar structure function
ζ_p p^{th}-order anomalous exponent

*Address all correspondence to this author.

$f^\dagger$ Complex conjugate of f
$\widetilde{f}$ Fourier transform of f
f^* Non-dimensional form of f

1 Introduction

The Richtmyer-Meshkov instability (RMI) occurs when fluid layers are impulsively accelerated in a direction normal to the interfaces between the layers, leading to the growth of any perturbations. The RMI is seen as a primary cause of inefficiency in attempts to produce energy via inertial confinement fusion (ICF) [1]. The capsule and fuel form a material interface, and the process of compression with intense x-ray laser light, generated through interaction of UV laser beams with the walls of a hohlraum, causes the propagation of a shock across this boundary, leading to the mixing of the fuel and capsule material and reducing yield. The instability has also been proposed as an important mechanism by which the mixing of fuel and oxidant in hypersonic aero-engines can be increased [2]. A comprehensive review of the state of the art of RMI studies is presented by Zhou [3, 4].

Here the focus will be on the evolution of spectral quantities, the scalar power spectrum, the scalar structure functions and the scaling of the structure functions. Integral quantities such as mixing width and mixedness are important to report as checks for numerical simulations, however spectral quantities allow an exploration of the mechanisms that lead to integral quantity evolution.

The integrated kinetic energy spectrum and density fluctuation spectrum in the RMI were studied by Schilling *et al*. [5] and Tritschler *et al*. [6] using data from numerical simulations.

Numerical experiments have explored some of the terms in the transport of kinetic energy in wavenumber space such as in Cook and Zhou [7] for the Rayleigh-Taylor instability (RTI) case and in Thornber and Zhou [8] for the RMI case, while a similar study of the scalar field has not been performed to the best of the authors' knowledge.

The scalar energy spectrum is explored in a number of experimental studies. Weber *et al*. [9] and Reese *et al*. [10] looked at the evolution of the scalar spectrum for the current initial condition (IC) after a single shock and found a small but growing wavenumber range with a $-\frac{5}{3}$ Kolmogorov scaling. Without access to time resolved data a connection to IC structure could not be made.

Structure functions of the density field of a gas curtain after shock are studied by Tomkins *et al*. [11] who found exponents greater than expected by Kolmogorov-Obukhov-Corrsin (KOC) scaling.

The current data set has previously been used to analyze the evolution of moments of the light gas mole fraction field by Noble *et al*. [12] and has been used as an experimental example of an iterative fluorescence correction scheme to extract estimates of the light gas mole fraction by Herzog *et al*. [13].

2 Experiment set-up

Experiments are conducted in a 9.1 m long, vertical, downward-firing shock tube with a square internal cross-section (25.4 cm on a side) shown in Fig. 1. The facility is described in detail by Anderson *et al* [14]. The 2-m long driver is filled with nitrogen to 80% of the rupture pressure of a 16-gauge steel diaphragm. The driven section is evacuated to 20 kPa, then a stagnation plane is formed by flowing the helium-acetone mixture downward from just below the diaphragm and flowing argon upward from just above the end wall of the shock tube. Chapman–Enskog relations are used to estimate mixture diffusivities such that the Schmidt number Sc is 0.09.

Once the stagnation plane is formed, and the pressure in the tube is 110 kPa, the vacuum system is turned on pulling excess gas from the vacuum line shown in Fig. 1 and a shear layer is created.

The experiment initial condition is generated using two planar jets to create a shear layer with argon injected above the stagnation plane and helium/acetone mixture below it. This configuration allows the resulting buoyancy forces to aid in the development of Kelvin-Helmholtz roll ups. This initial condition has been used in previous studies in this facility [9, 10].

The pressure inside the tube is now at a steady state with excess gas being taken out at the interface by the vacuum system. This steady state is allowed to persist for 15 minutes to allow any air that was mixed in with the desired gas to be extracted from the system.

A pulse-burst laser system is used to create a pulse train of 10 ms duration at a repetition rate of 20 kHz. The system amplifies the output of an Nd:YVO_4 oscillator laser in Nd:YAG amplification stages. The fourth harmonic output at 266 nm is used in the experiments with an average energy of 30 mJ per pulse for each pulse in the burst. The pulse train is passed through a spherical lens and a cylindrical lens to create a diverging laser sheet that spans the entire width of the shock tube 1 m above the end wall of the tube. This laser sheet excites the acetone present in the light gas mixture causing it to fluoresce. A Phantom V1840 high-speed camera with a 1 μs exposure is used to capture the resulting fluorescence signal. Camera linearity was previously measured in a light-box, and the results are used to correct PLIF measurements.

To generate a shock, the steel diaphragm is ruptured. Figure 2 shows a combined experimental and theoretical z-t diagram for experiment HS1 (Table 1). The reference axes are oriented so that the reflected shock (green) is shown

propagating in the positive z-direction. This reflected shock interacts with the mixing layer at time t=0; a shock is transmitted while a rarefaction is reflected which then reflects off the end wall of the shock tube and interacts with the mixing layer. This interaction causes the centroid of the mixing layer to become stationary within the field of view. At 3 ms, there is a compression wave propagating vertically downward which is the transmitted shock reflecting off the contact surface between the driver gas and the driven gas. This causes the mixing layer to begin propagating downward while also compressing the mixing layer.

The parameters of the three experiments are described in Table 1, here M_s is the initial shock Mach number, A^+ is the post-shock Atwood number, A^{++} is the post-reshock Atwood number and Re_{h0} is the resulting initial Reynolds number.

	M_s	A^+	A^{++}	Re_{h0}
HS1	1.94	0.253	0.247	4.7x10^4
HS2	1.90	0.306	0.312	7.8x10^4
HS3	1.95	0.244	0.236	1.9x10^4

Table 1: Parameters of high-speed experiments, adapted from Noble *et al*. [12] where in that paper HS1 is HS4, HS2 is HS6 and HS3 is HS8.

3 Non-Dimensionalisation of Governing Equations

Here the transport equation for the light gas mole fraction, ξ, is transformed into a deforming frame of reference that follows the centroid of the interface and scales with the mixing width. This is to allow an identification of terms and a comparison between experiments. The functional form of this transformation is $\xi(x,z,t) \rightarrow \xi(x^*,z^*,h^*)$ with $x^* = \frac{x}{W}$, $z^* = \frac{z-z_0}{h}$ and $h^* = \frac{h}{h_0}$ where x is the span-wise coordinate and z is the stream-wise coordinate, W is some representative spanwise length scale (here it is the shock tube width), $z_0 = 4\int_{-\infty}^{\infty} z\overline{\xi}(1-\overline{\xi})dz^*$ is the time-varying location of the mole-fraction weighted centroid of the mixing layer, h is the time-varying mixing thickness and h_0 is the initial mixing thickness immediately after the reflected shock has fully traversed the mixing layer. Introducing the spanwise average in the x-direction of some function f as

$$\overline{f} = \frac{1}{W}\int_0^W f\, dx \tag{1}$$

such that $f = \overline{f} + f'$, then the mixing thickness is defined as

$$h = 4\int_{-\infty}^{\infty} \overline{\xi}(1-\overline{\xi})\, dz. \tag{2}$$

Our data analysis starts with the transport equation for ξ

$$\frac{\partial \xi}{\partial t} + \overrightarrow{\nabla}\cdot\overrightarrow{u}\xi = \mathcal{D}\overrightarrow{\nabla}^2\xi, \tag{3}$$

where $\overrightarrow{u}$ and $\mathcal{D}$ are the velocity and mass diffusivity, respectively. Specialising to 2D, and introducing the following non-dimensionalisation

$$\overrightarrow{u}^* = \frac{\overrightarrow{u} - \overrightarrow{V_0}}{\dot{h}} \tag{4}$$

where V_0 is the bulk velocity of the interface in the lab fixed frame, and when expanded, Eq.3 becomes

$$\frac{\partial \xi}{\partial \ln h^*} - z^* \frac{\partial \xi}{\partial z^*} + \frac{\partial u^* \xi}{\partial x^*} \frac{h}{W} + \frac{\partial w^* \xi}{\partial z^*} = \frac{1}{Re_h Sc} \left[\frac{\partial^2 \xi}{\partial x^{*2}} (\frac{h}{L})^2 + \frac{\partial^2 \xi}{\partial z^{*2}} \right]. \tag{5}$$

This was derived in appendix A of Noble *et al*. [12] and is the form of transport equation used by Ristorcelli *et al*. [15] where $Re_h = \frac{h\dot{h}}{\nu}$ is the outer scale Reynolds number and $Sc = \frac{\nu}{\mathcal{D}}$ is the Schmidt number with ν being the kinematic viscosity.

3.1 Power Spectrum Evolution

Starting with equation 5, taking the Fourier transform, $\widetilde{\xi} = \mathcal{F}[\xi]$, and multiplying by the complex conjugate $\widetilde{\xi}^\dagger$, the evolution equation for the scalar power spectra can be found to be

$$\frac{\partial E_\xi}{\partial \ln h^*} - z^* \frac{\partial E_\xi}{\partial z^*} + \mathcal{P} + \mathcal{T}_\xi = \mathcal{D}_\xi - \chi_\xi \tag{6}$$

with all terms defined in Table 2.

This is a similar form to the transport equation of the inhomogenous kinetic energy spectrum found by Andrade *et al*. [16]. Velocity is not directly measured in these experiments, so the production and transport terms cannot be separated and are combined in a fluctuating transport and production flux, π^*_ξ. Utilising the time evolution of E_ξ, an estimate of π^*_ξ can be obtained. The transport term, the flux, the diffusion spectrum and the dissipation spectrum are then integrated over dimensionless time ($\ln h^*$) to the latest time available in all 3 experiments, $h^* = 8$, resulting in Eqs. (7)-(10). These allow an analysis of the different contributions to the change in the energy spectra.

$$T_\xi(z^*, k_x^*) = \int_0^{\ln 8} z^* \frac{\partial E_\xi}{\partial z^*} \, d\ln h^* \tag{7}$$

$$\Pi_\xi(z^*, k_x^*) = \int_0^{\ln 8} \int_0^{k_x^*} \mathcal{P} + \mathcal{T} \, dk_x^* \, d\ln h^* \tag{8}$$

$$D_\xi(z^*, k_x^*) = \int_0^{\ln 8} \mathcal{D}_\xi \, d\ln h^* \tag{9}$$

$$X_\xi(z^*, k_x^*) = \int_0^{\ln 8} \chi_\xi \, d\ln h^* \tag{10}$$

This leads to a form of the scalar power spectrum that has been integrated over dimensionless time shown in Eq. (11). Each of the terms can be considered separately to identify its contribution to the total change in energy.

$$\Delta E_\xi - T_\xi + \frac{\partial \Pi_\xi}{\partial k_x^*} = D_\xi - X_\xi \tag{11}$$

3.2 Structure Function Evolution

Defining the p^{th}-order structure function as $S_{\xi,p}(z^*, r^*, h^*) = \overline{\delta\xi^p} = \overline{(\xi(x^* + r_x^*) - \xi(x^*))^p}$, and using Eq. 5, a Karman-Howarth-Monin type transport equation can be derived following the example of Hill [17] where $r_x^* = \frac{r_x}{W}$ is the two-point separation in the spanwise direction

$$\frac{\partial S_{\xi,p}}{\partial \ln h^*} - z^* \frac{\partial S_{\xi,p}}{\partial z^*} + \mathcal{T}_{S,p} + \mathcal{P}_{S,p} = \mathcal{D}_{S,p} - \chi_{S,p} \tag{12}$$

	E_ξ	$S_{\xi,p}$
Production $\mathcal{P}$	$\left(\widetilde{w}\widetilde{\xi}^\dagger + \widetilde{w}^\dagger\widetilde{\xi}\right)\frac{\partial\overline{\xi}}{\partial z^*}$	$p\ \overline{\delta\xi^{p-1}\ \delta w^*}\frac{\partial\overline{\xi}}{\partial z^*}$
Transport $\mathcal{T}$	$ik_x^*\left(\widetilde{u\xi}\widetilde{\xi}^\dagger + \widetilde{u\xi}^\dagger\widetilde{\xi}\right)\frac{h}{W} + \left(\frac{\partial\widetilde{w\xi}}{\partial z^*}\widetilde{\xi}^\dagger + \frac{\partial\widetilde{w\xi}^\dagger}{\partial z^*}\widetilde{\xi}\right)$	$\frac{\partial}{\partial r^*}\left[p\overline{\delta(u^*\xi')\ \delta\xi^{p-1}}\right] + \frac{\partial}{\partial z^*}\left[p\overline{\delta(w^*\xi')\ \delta\xi^{p-1}}\right]$
Diffusion $\mathcal{D}$	$\frac{1}{Re_hSc}\left[-2k^{*2}\left(\frac{h}{W}\right)^2 E_\xi + \frac{\partial^2 E_\xi}{\partial z^{*2}}\right]$	$\frac{1}{Re_hSc}\left[\frac{\partial^2 S_{\xi,p}}{\partial r^{*2}}\left(\frac{h}{W}\right)^2 + \frac{\partial^2 S_{\xi,p}}{\partial z^{*2}}\right]$
Dissipation χ	$\frac{1}{Re_hSc}\left[\frac{\partial\widetilde{\xi}}{\partial z^*}\frac{\partial\widetilde{\xi}^\dagger}{\partial z^*}\right]$	Equation 13

Table 2: Terms in power spectra and structure function transport

with all terms again defined in Table 2.

$$\chi^*_{S,p} = \frac{1}{Re_hSc}\Bigg[p(p-1)\overline{\delta\xi^{p-2}\left(\frac{\partial\,\delta\xi}{\partial z^*}\right)^2} + p(p-1)\overline{\delta\xi^{p-2}\left(\frac{\partial\,\delta\xi}{\partial r^*}\right)^2 + \delta\xi^{p-2}\left(\frac{\partial\,\delta\xi}{\partial X^*}\right)^2}\left(\frac{h}{W}\right)^2 - \overline{p\delta\xi^{p-1}\left(\frac{\partial\,(\xi_2+\xi_1)}{\partial r^*\partial X^*}\right)}\Bigg] \quad (13)$$

4 Results and Discussion

The results presented here use measurements from three experiments which are a subset of a set of eight experiments described in Noble *et al*. [12], sharing experimental setups and IC creation with Weber *et al*. [9] and Reese *et al*. [10]. These three are chosen for study here as they have similar Atwood and Mach number but different IC modal content. The shocked and reshocked Atwood number and initial Reynolds number for the subset of experiments are listed in Table 1, the evolution of the light gas mole fraction in each of the three experiments is shown in Fig.3 and the IC of each experiment is shown in Fig. 4.

In Fig. 5 the dimensionless thickness h^* is plotted against the dimensionless time $\tau = (t - t_{rs})\frac{\dot{h}_0}{h_0}$ for each of the three experiments, where t_{rs} is when the reflected shock has fully traversed the mixing layer. A period of linear growth with time, $h^* - 1 = \tau$ (the dotted line in Fig.(5)), is seen as expected after reshock with the appearance of a power law behaviour for HS1 and HS3 more reminiscent of singly shocked behaviour.

4.1 Energy Spectrum

Following Schilling et al [18], the energy spectrum is integrated over the mixing layer such that $\Lambda_\xi(k_x^*, h^*) = \int_{-\infty}^{\infty} E_\xi\, dz^*$ (here the limits are $\pm\infty$ rather than the bubble and spike heights). Figure 6 plots Λ_ξ, which is a measure of the magnitude of fluctuations at a given wavenumber with a smaller magnitude meaning weaker fluctuations from the mean and a more fully mixed state.

The IC of HS2 in Fig. 4 visibly shows a broader range of scales and larger x-gradients which leads to a period of strong mixing immediately after the passage of the reflected shock.

HS1 and HS3 show qualitative similarities in Fig. 6. HS1 and HS3 begin with smaller values of Λ_ξ at higher wavenumbers as opposed to HS2 which starts at higher values that subsequently dissipate.

In the current data the scaling at higher wavenumbers does not appear to be IC dependent.

All 3 experiments arguably show regions of KOC $-\frac{5}{3}$ scaling, which would identify an inertial-convective regime, however a region closer to $-\frac{11}{3}$ covers a much larger range for all 3 experiments. Batchelor *et al*. [19] propose a scaling of $-\frac{17}{3}$ for a Schmidt number $Sc << 1$ which corresponds to the inertial-diffusive regime, whereas here we have $Sc = 0.1$. They propose that small scale mixing is independent of large scale straining. A review of work on turbulent mixing is presented by Sreenivasan [20] where the different scaling regions for varying Sc for passive scalars are elaborated on.

Gibson [21] argues that the assumption of Batchelor that low wavenumbers of the scalar spectrum are not affected by larger scale straining is not necessarily a good approximation and instead of a $-\frac{17}{3}$ slope they find a -3 slope for the inertial-diffusive range. Frisch and Wirth [22] however find that for a white-in-time velocity field with an inertial range scaling of $-\frac{5}{3}$, the inertial diffusive range should have a $-\frac{11}{3}$ scaling. Although this scaling matches the observed scaling, its base assumption of a white-in-time velocity field doesn't match observed velocity field correlations that have non-zero integral time scales.

These attempts at developing scaling relations are for passive scalar quantities whose structure does not effect the dynamics of the velocity field. In RMI flows the light gas mole-fraction is an active scalar. To the authors knowledge there isn't an accepted universal model of active scalar scaling.

Three representative wavenumbers are highlighted in Fig.6, the integral scale $L = \frac{\int_{-\infty}^{\infty} k^{-1} E_\xi dk}{\int_{-\infty}^{\infty} E_\xi dk}$, the scalar taylor scale $\lambda^2 = \frac{\overline{\xi'^2}}{\overline{\left(\frac{\partial \xi'}{\partial x_i}\right)^2}}$ and an estimate of the scalar Kolmogorov scale, which is the Obukhov–Corrsin scale, using the isotropic homogeneous relation $\lambda = \sqrt{10}\eta^{2/3}L^{1/3}$. For all 3 experiments the Taylor scale seems to be a demarcation point between the two scaling regions, an inertial range and an inertial diffusive range, with the OC scale estimated as being below the measurement scale ($\Delta = 0.245$ mm).

4.2 Partition of Energy

Equation (11) describes the partition of scalar energy over a given change in time. The individual terms are plotted in Fig. 7. The time period represented here begins after the reflected shock has fully traversed the mixing layer, it includes the passage of an expansion wave and ends at the latest dimensionless time available before the arrival of a compression wave.

The total change in energy, ΔE_ξ, is concentrated at larger wavelengths on the order of the shocktube width which correspond to the growth and transport of bulk structures. This is codified in the plots of bulk transport, T_ξ. The diffusion, D_ξ doesn't create or destroy energy, only transporting it within the mixing layer. χ_ξ is the dissipation term and represents the removal of scalar energy which appears to occur at shorter wavelengths.

The previous terms can be directly estimated from the measurements of the light gas mole fraction. The fluctuating flux Π_ξ, must be inferred from the time evolution of the power spectrum. Unfortunately the fluctuating transport and the production term cannot be separated here.

Thornber and Zhou [8] remarked that transport was asymmetric about the center of the mixing layer, here a similar argument can be made, however it does seem IC dependent with HS1 and HS3 appearing to behave more symmetrically, whereas HS2 does have dominant transport on the spike side of the mixing layer.

Cook and Zhou [7] calculate the time varying dissipation, production and transport in non-scaling coordinates and find similar trends, with dissipation occurring at smaller wavelengths and production and transport reaching peaks at longer wavelengths.

4.3 Structure Function

Figure 8 shows the integrated 2$^{\text{nd}}$-order structure function $Z_{\xi,2} = \int_{-\infty}^{\infty} S_{\xi,2} dz^*$. This is closely related to the energy spectrum and describes the energy contained at a given scale. The plots of $Z_{\xi,2}$ support the same analysis as the plots of Λ_ξ where HS2 begins with more energy at the smaller scales which subsequently dissipate while HS1 and HS3 begin with less energy at small scales and energy subsequently transfers down from larger scales.

The reference scales shown in Fig 8 are the KOC scaling of 2/3 and a scaling of unity that very closely matches the observed slope at the latest times.

4.4 Anomalous Exponent

KOC scaling proposes that the exact result of Kolmogorov's $4/5$ law can be extended beyond the 3rd order for which it was derived such that the exponent, ζ_p, of the structure function, $Z_{\xi,p} \propto r^{*\zeta_p}$, is equal to $\frac{p}{3}$.

Figure 9 plots ζ_p, the exponent of the p^{th} order integrated scalar structure function. Kraichnan [23] proposes a scaling of $\zeta_p = \frac{1}{2}[\sqrt{6p+4} - 2]$ using a model for the diffusion of the passive scalar. The Kraichnan (K) behaviour of $\sqrt{p}$ at large p works well for HS2, shown in Fig.(10), where the higher initial Reynolds number allows the flow to become more fully mixed. HS1 and HS3 both have ICs far from KOC scaling but seem to be trending toward this scaling as time progresses.

5 Conclusions

Evolution equations for the scalar power spectrum and the n^{th}-order scalar structure function in a reshock RMI environment are presented. The power spectrum evolution equation is used to estimate the structure and value of the combined fluctuating production and transport term.

All three experiments display some range of inertial range KOC scaling in the power spectrum, but a much larger region of $-\frac{11}{3}$ points toward an inertial-diffusive range.

The partition of energy shows a strong IC dependence on the structure of the different contributing terms. Production and transport is shown to be strongest above and below the center of the mixing layer. HS2 has the largest initial Reynolds number and has the highest contribution due to dissipation with HS3 having the lowest initial Reynolds number and correspondingly a smaller contribution due to dissipation.

The initial anomalous exponents for HS1 and HS3 begin far away from KOC scaling but appear to tend toward this scaling as the mixing layer grows. The exponent of HS2 is initially close to KOC scaling, however the square root behaviour predicted by Kraichnan appears to more closely match the order dependence at later times.

References

[1] Lindl, J. D., Amendt, P., Berger, R. L., Glendinning, S. G., Glenzer, S. H., Haan, S. W., Kauffman, R. L., Landen, O. L., and Suter, L. J., 2004. "The physics basis for ignition using indirect-drive targets on the National Ignition Facility". *Phys. of Plasmas,* **11**(2), Feb., pp. 339–491.

[2] Marble, F. E., Hendricks, G. J., and Zukoski, E. E., 1989. "Progress Toward Shock Enhancement of Supersonic Combustion Processes". *Turbulent Reactive Flows,* **40**, p. 26.

[3] Zhou, Y., 2017. "Rayleigh-Taylor and Richtmyer-Meshkov instability induced flow, turbulence, and mixing. I". *Physics Reports,* **720-722**, Dec., pp. 1–136.

[4] Zhou, Y., 2017. "Rayleigh-Taylor and Richtmyer-Meshkov instability induced flow, turbulence, and mixing. II". *Physics Reports,* **723-725**, Dec., pp. 1–160.

[5] Schilling, O., Latini, M., and Don, W. S., 2007. "Physics of reshock and mixing in single-mode Richtmyer-Meshkov instability". *Phys. Rev. E,* **76**(2), Aug.

[6] Tritschler, V., Olson, B., Lele, S., Hickel, S., Hu, X., and Adams, N., 2014. "On the richtmyer–meshkov instability evolving from a deterministic multimode planar interface". *JFM,* **755**, p. 429–462.

[7] Cook, A. W., and Zhou, Y., 2002. "Energy transfer in Rayleigh-Taylor instability". *Phys. Rev. E,* **66**(2), Aug.

[8] Thornber, B., and Zhou, Y., 2012. "Energy transfer in the richtmyer-meshkov instability". *Phys. Rev. E,* **86**, Nov, p. 056302.

[9] Weber, C. R., Haehn, N. S., Oakley, J. G., Rothamer, D. A., and Bonazza, R., 2014. "An experimental investigation of the turbulent mixing transition in the Richtmyer-Meshkov instability". *JFM,* **748**, June, pp. 457–487.

[10] Reese, D., Oakley, J., Navarro-Nunez, A., Rothamer, D., Weber, C., and Bonazza, R., 2018. "Simultaneous concentration and velocity field measurements in a shock-accelerated mixing layer". *JFM,* **849**(10), Oct., p. 541–575.

[11] Tomkins, C. D., Balakumar, B. J., Orlicz, G., Prestridge, K. P., and Ristorcelli, J. R., 2013. "Evolution of the density self-correlation in developing Richtmyer-Meshkov turbulence". *JFM,* **735**, Nov., pp. 288–306.

[12] Noble, C. D., Herzog, J. M., Ames, A. M., Oakley, J., Rothamer, D. A., and Bonazza, R., 2020. "High speed plif study of the richtmyer-meshkov instability upon re-shock". *Physica D: Nonlinear Systems*.

[13] Herzog, J. M., Ames, A., Noble, C., Oakley, J., Bonazza, R., and Rothamer, D. A., 2019. "Iterative correction of shocked acetone high-speed PLIF measurements in the Richtmyer-Meshkov instability". *Proceedings of the International Symposium on Shock Waves,* **32**.

[14] Anderson, M., Puranik, B., Oakley, J., Brooks, P., and Bonazza, R., 2000. "Shock tube investigation of hydrodynamic issues related to inertial confinement fusion". *Shock Waves,* **10**(5), Nov., pp. 377–387.

[15] Ristorcelli, J. R., and Clark, T. T., 2004. "Rayleigh-Taylor turbulence: self-similar analysis and direct numerical simulations". *JFM,* **507**, May, pp. 213–253.

[16] Andrade, J. R., Martins, R. S., Mompean, G., Thais, L., and Gatski, T. B., 2018. "Analyzing the spectral energy cascade in turbulent channel flow". *Physics of Fluids,* **30**(6), p. 065110.

[17] Hill, R. J., 2002. "Exact second-order structure-function relationships". *JFM,* **468**, p. 317–326.

[18] Schilling, O., and Latini, M., 2010. "High-order WENO simulations of three-dimensional reshocked Richtmyer-Meshkov instability to late times: dynamics, dependence on initial conditions, and comparisons to experimental data". *Acta Mathematica Scientia,* **30**(2), pp. 595–620.

[19] Batchelor, G. K., Howells, I. D., and Townsend, A. A., 1959. "Small-scale variation of convected quantities like temperature in turbulent fluid part 2. the case of large conductivity". *JFM,* **5**(1), p. 134–139.

[20] Sreenivasan, K. R., 2019. "Turbulent mixing: A perspective". *Proceedings of the National Academy of Sciences,* **116**(37), pp. 18175–18183.

[21] Gibson, C. H., 1968. "Fine structure of scalar fields mixed by turbulence. ii. spectral theory". *The Physics of Fluids,* **11**(11), pp. 2316–2327.

[22] Frisch, U., and Wirth, A., 1996. "Inertial-diffusive range for a passive scalar advected by a white-in-time velocity field". *Europhysics Letters (EPL),* **35**(9), sep, pp. 683–688.

[23] Kraichnan, R. H., 1994. "Anomalous scaling of a randomly advected passive scalar". *Phys. Rev. Lett.,* **72**, Feb, pp. 1016–1019.

List of Figures

List of Tables

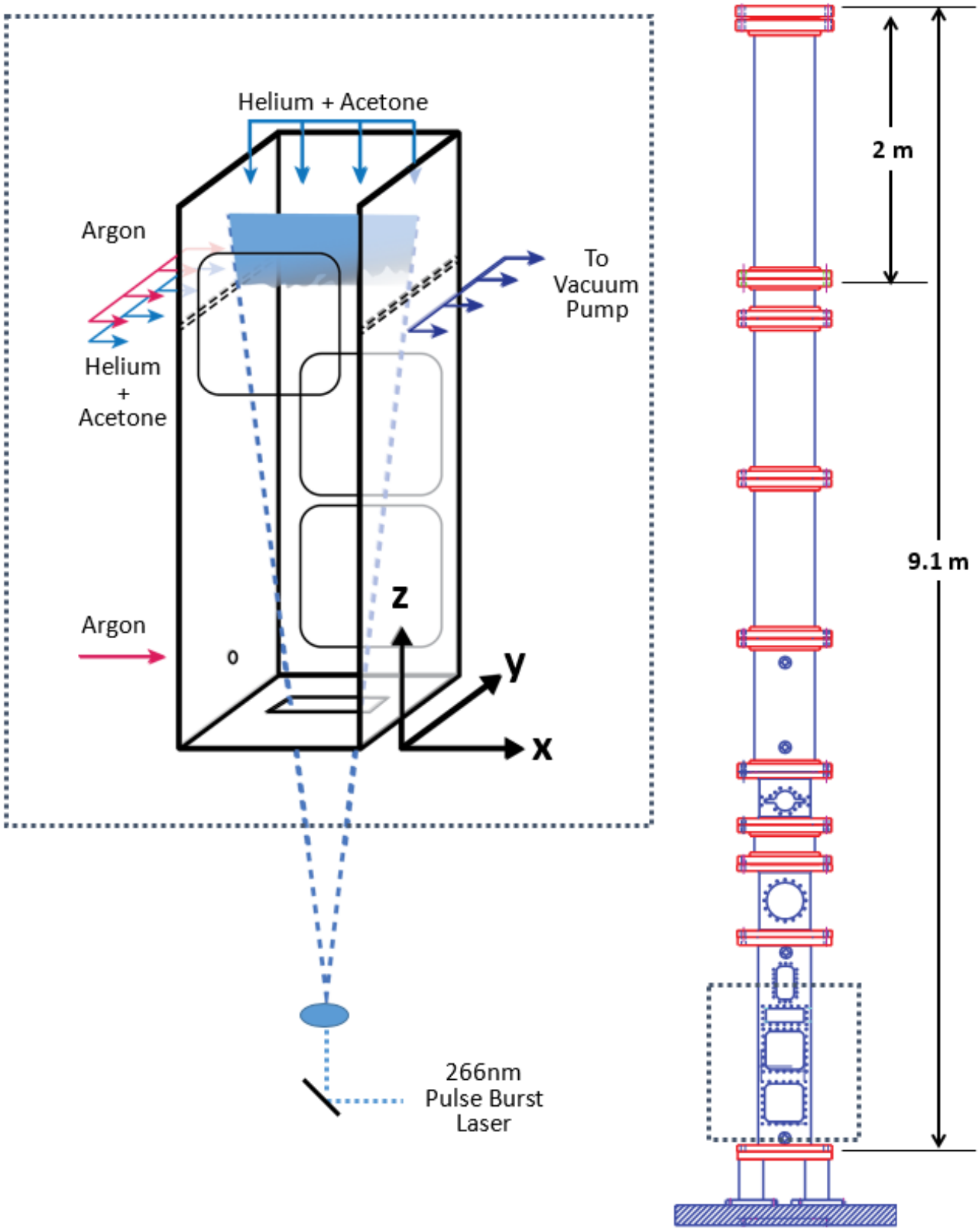

Fig. 1: Diagram of test section showing coordinate system and experiment layout.

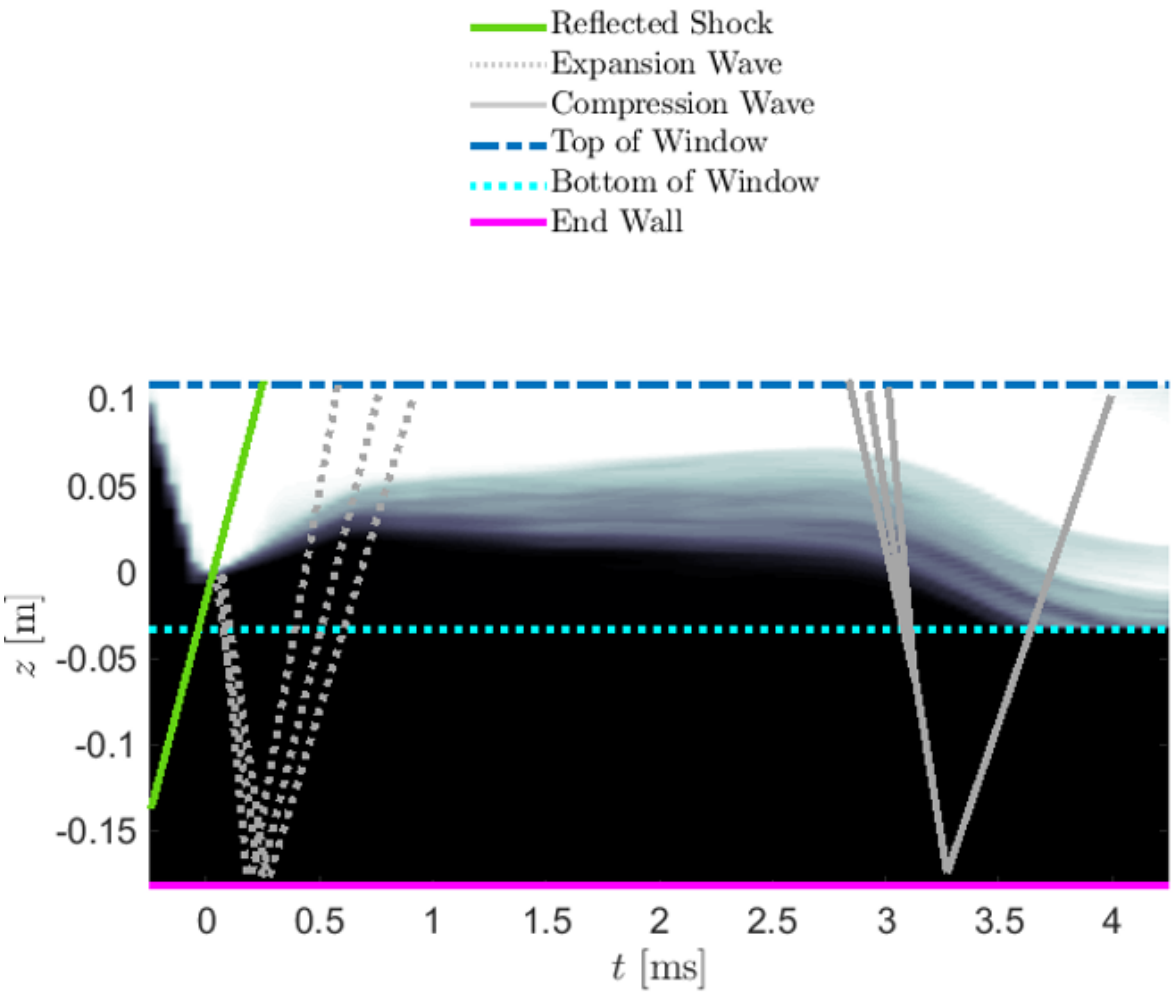

Fig. 2: Combined experimental and theoretical z-t diagram showing the spanwise averaged light gas mole fraction as a function of z and t from HS1 (Table 1). $z = 0$ and $t = 0$ represent the spatial and temporal location of the interaction of the reflected shock with the interface. The overlaid wave pattern is generated from 1D gas dynamics and shows the initial shock, reflected rarefaction and a compression train from the shock reflecting off the contact surface above the window (the contact surface being the surface separating the driver gas from the driven gas.)

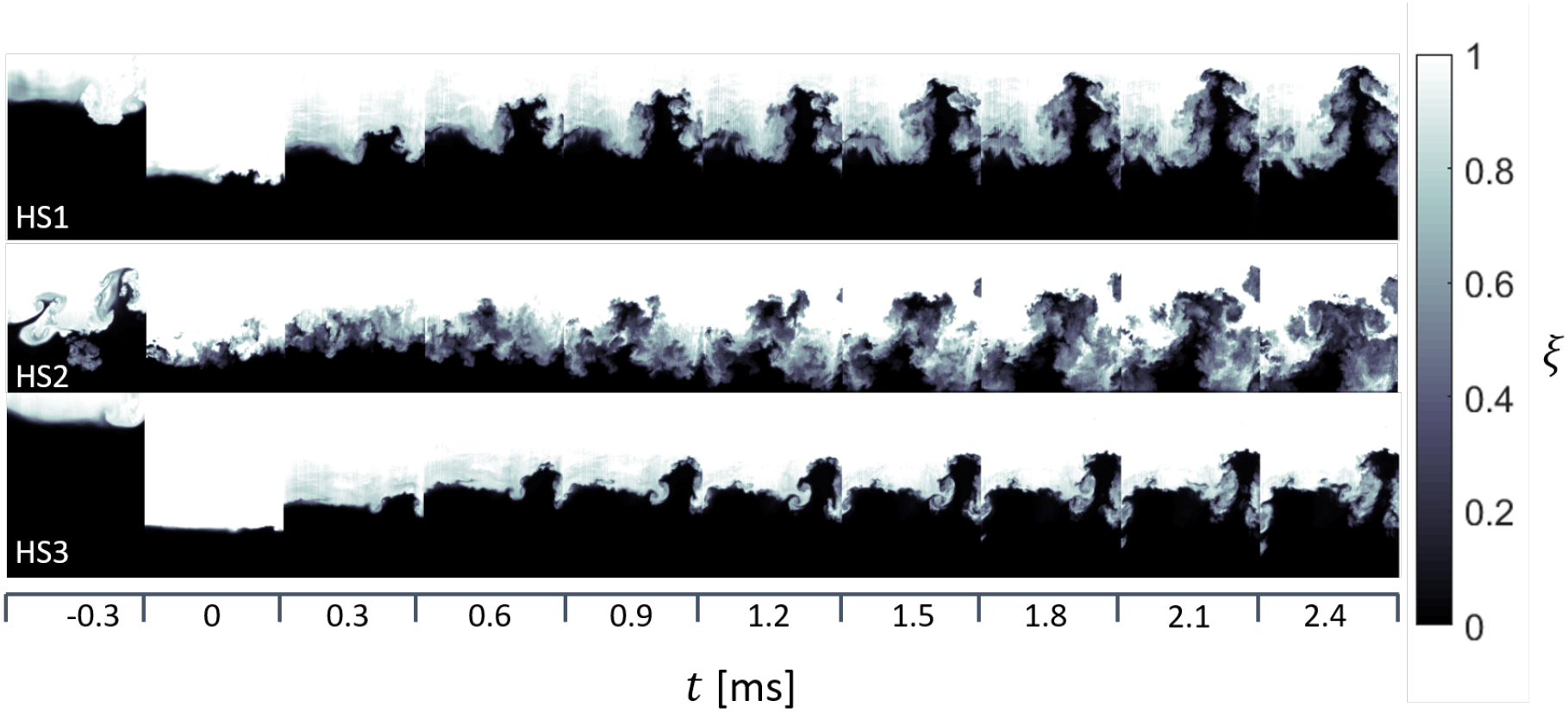

Fig. 3: Example mole fraction fields evolving with time from 3 experiments. Details of each run are given in Table 1.

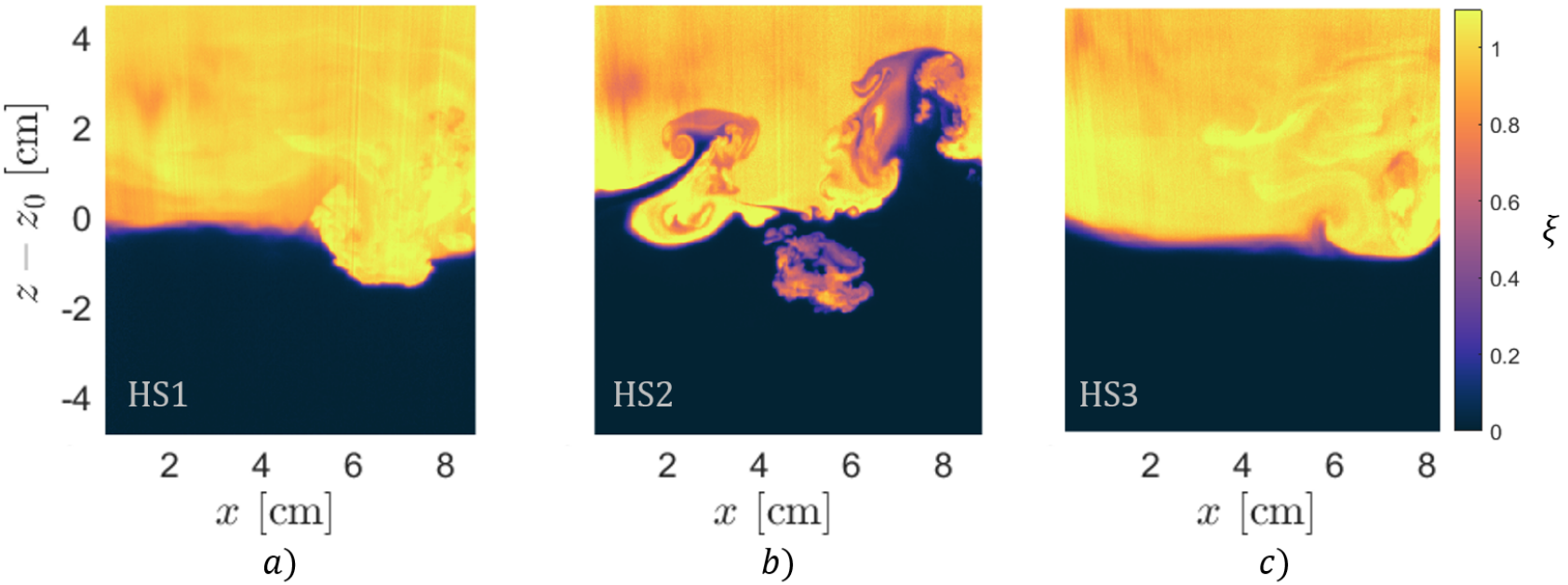

Fig. 4: Initial conditions before interaction with reflected shock wave. Details of each run are given in Table 1. a) HS1, b) HS2 and c) HS3.

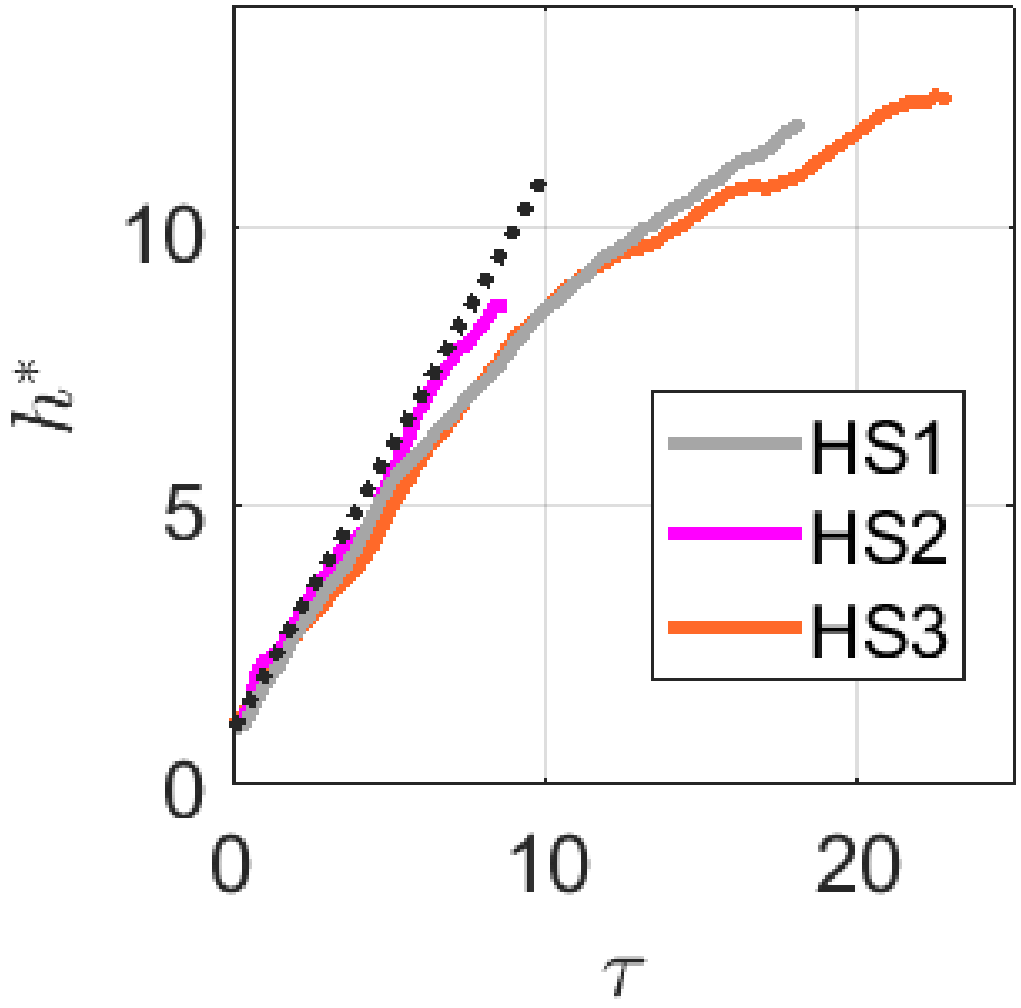

Fig. 5: Non-dimensional height vs non-dimensional time for the three experiments.

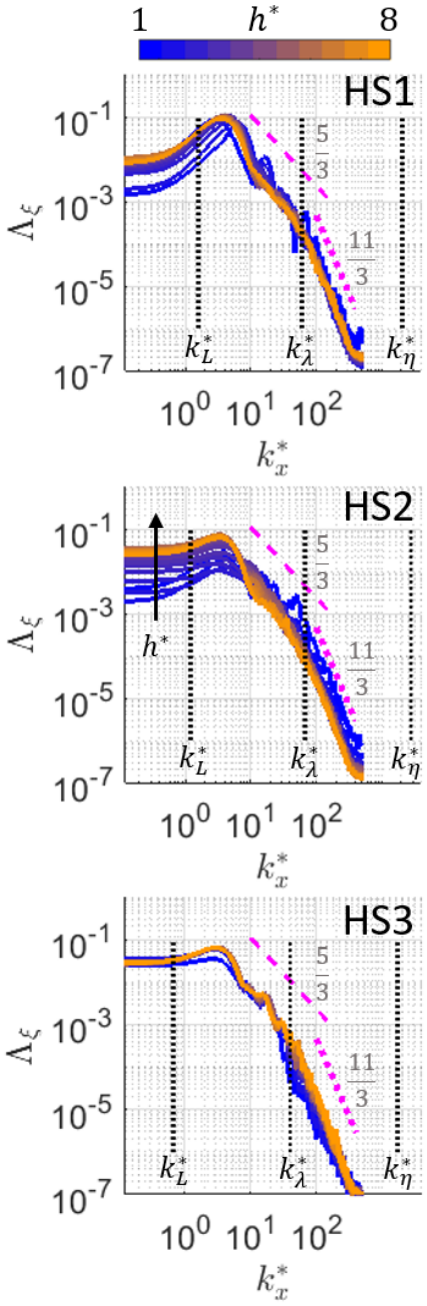

Fig. 6: Profiles of the integrated power spectrum.

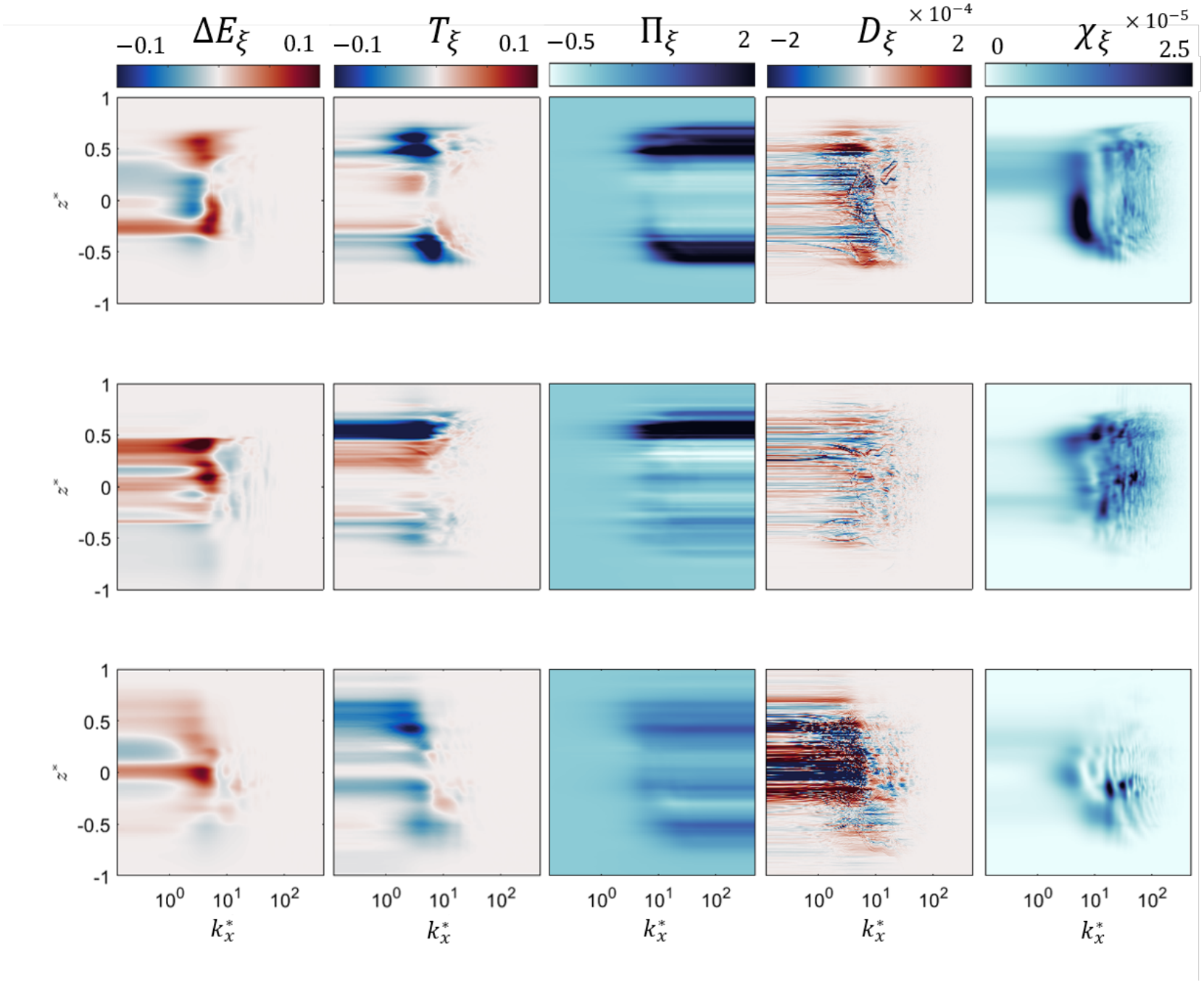

Fig. 7: total change in scalar energy from $h^* = 1$ to $h^* = 8$.Top: HS1, middle: HS2 and bottom: HS3.

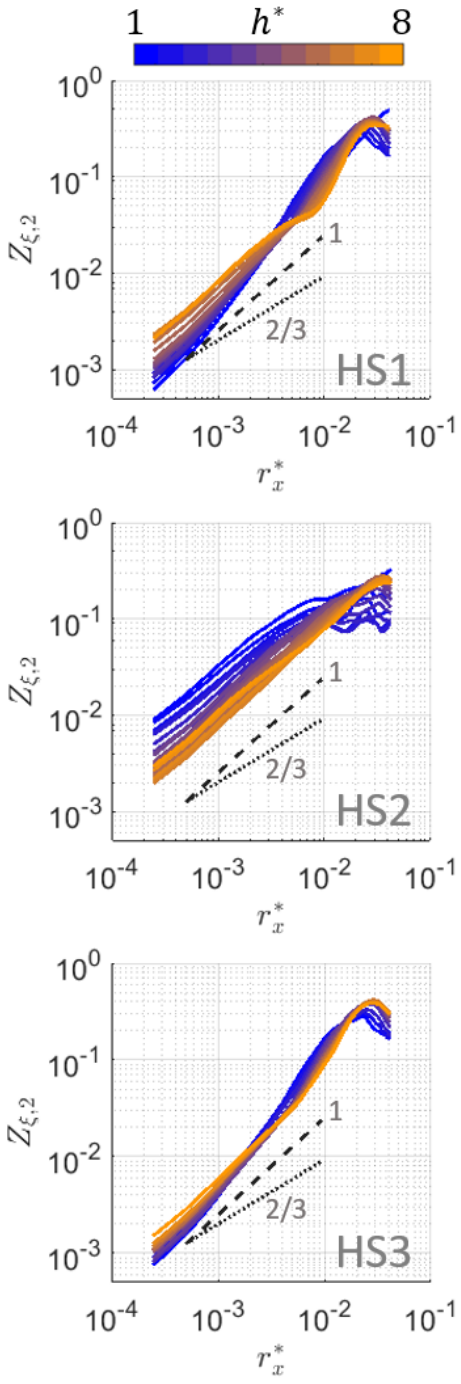

Fig. 8: Time evolution of profiles of $Z_{\xi,2}$, the integrated 2nd order structure function.

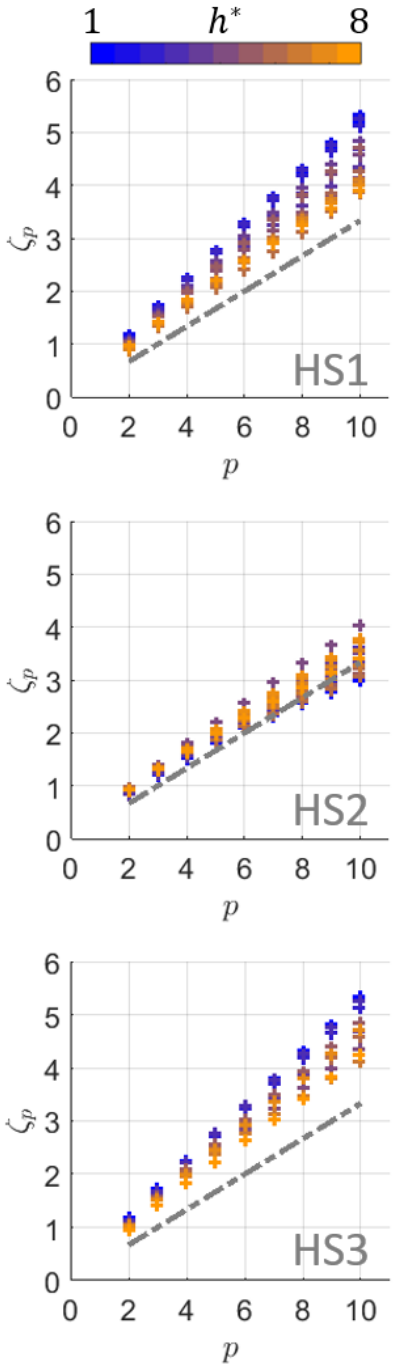

Fig. 9: Time evolution of the anomalous exponent of the structure function of order p. (- - - - - - KOC scaling $\frac{p}{3}$)

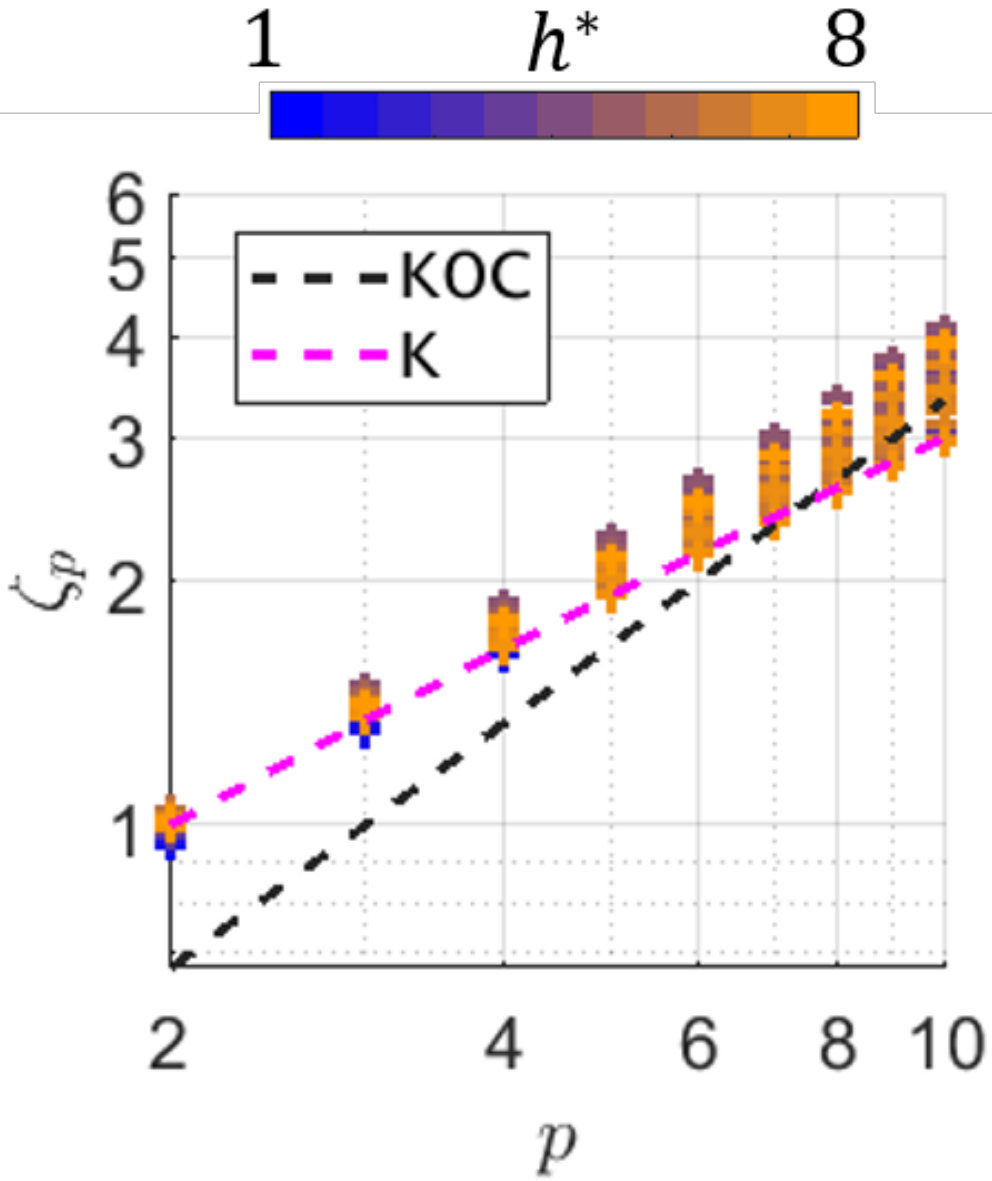

Fig. 10: Log-log plot of the anomalous exponent of HS2 showing the difference between KOC and K scaling